HIV-1 Integrase Catalytic Core: Molecular Dynamics and Simulated Fluorescence Decays

Cyril Laboulais,* Eric Deprez,* Hervé Leh,† Jean-François Mouscadet,† Jean-Claude Brochon,* and Marc Le Bret*

*Laboratoire de Biotechnologies et de Pharmacologie Génétique Appliquée (UMR8532 Centre National de la Recherche Scientifique), Ecole Normale Supérieure de Cachan, 94235 Cachan, and †Laboratoire de Physicochimie et de Pharmacologie des Macromolécules Biologiques (UMR8532 Centre National de la Recherche Scientifique), Institut Gustave Roussy, 94805 Villejuif, France

ABSTRACT Two molecular dynamics simulations have been carried out on the HIV-1 integrase catalytic core starting from fully determined crystal structures. During the first one, performed in the absence of divalent cation (6-ns long), the catalytic core took on two main conformations. The conformational transition occurs at approximately 3.4 ns. In contrast, during the second one, in the presence of Mg^{2+} (4-ns long), there were no such changes. The molecular dynamics simulations were used to compute the fluorescence intensity decays emitted by the four tryptophan residues considered as the only chromophores. The decay was computed by following, frame by frame, the amount of chromophores that remained excited at a certain time after light absorption. The simulation took into account the quenching through electron transfer to the peptide bond and the fluorescence resonance energy transfer between the chromophores. The fit to the experimental intensity decays obtained at 5°C and at 30°C is very good. The fluorescence anisotropy decays were also simulated. Interestingly, the fit to the experimental anisotropy decay was excellent at 5°C and rather poor at 30°C. Various hypotheses such as dimerization and abnormal increase of uncorrelated internal motions are discussed.

INTRODUCTION

Fluorescence intensity and anisotropy decays of proteins from low concentration samples can be accurately measured using modern techniques provided they contain an aromatic amino acid such as tryptophan (Trp), tyrosine, or phenylalanine. However, until recently, the data could not be easily interpreted in part due to their extraordinary sensitivity to the environment. Consequently, fluorescence techniques have contributed much less to structural determinations than molecular modeling, NMR, let alone x-ray crystallography. When it is possible to predict fluorescence properties from a conformation, back-calculations can be iterated, finally yielding a refined insight into the structures and dynamics of proteins in solution.

X-ray, time-resolved fluorescence and molecular dynamics (MD) simulation have recently been successfully combined to study the Human Immunodeficiency Virus-1 (HIV-1), protease/inhibitor complex (Ringhofer et al., 1999). Binding of the inhibitor induced a faster decay of both the experimental and computed protease fluorescence anisotropy decays. The total anisotropy decay of the four Trp system was assumed to be a linear combination of individual fluorescence anisotropy decays that were deduced from the trajectories of each Trp transition moment according to the pioneer work of Ichiye and Karplus (1983). There was no attempt to take into account excitation migration among Trp residues, probably because transfer rates must be evaluated, and these, at their turn, depend on fluorescence lifetimes.

In this paper, both intensity and anisotropy decays are simulated, which implies that most of Trp de-excitation processes are evaluated. This is now possible thanks to recent contributions. First, eight amino-acid side chains may act as quenchers of the Trp fluorescence (Chen and Barkley, 1998). Second, the peptide bond itself was recognized as a quencher of the indole fluorescence (Chen et al., 1996). The electron transfer rate essentially depends on the proximity of the indole ring CE3 atom to the carbon atom of the peptide bond carbonyl (Sillen et al., 2000). This role was delineated by comparison of experimental lifetimes and short MD simulations of a unique Trp-containing protein. In the present work, the method is applied to a protein containing four Trp residues, namely the HIV-1 integrase (IN) catalytic core. At each step of the dynamics, the instantaneous fluorescence lifetime was computed. Moreover, the probability that a chromophore remained excited during a given time was computed separately for each absorption time, then averaged over all possible absorption times. Resonance energy transfer makes the simulation more complex and was introduced in the calculations to predict not only the fluorescence intensity decays but also the fluorescence anisotropy decays from the trajectories.

The integration of a proviral cDNA into host DNA is a critical step in the life cycle of the HIV-1 because it ensures expression and perpetuation of the viral genome (Sakai et al., 1993). This essential reaction is catalyzed by the viral enzyme IN that has been shown to be necessary and sufficient for the integration reaction in vitro (Bushman et al., 1990; Brown, 1990). The integration function is composed of two steps, both involving the nucleophilic attack of a

---

Received for publication 18 January 2001 and in final form 10 April 2001.

Address reprint requests to Marc Le Bret, LBPA, ENS Cachan, 61 avenue du Président Wilson, 94235 Cachan, France. Tel.: 33-1-47-40-59-97; Fax: 33-1-47-40-24-79; E-mail: mlebret@lbpa.ens-cachan.fr.

© 2001 by the Biophysical Society

0006-3495/01/07/473/17 $2.00

phosphoester bond by the lone pair of a hydroxyl group. In the first step, called processing reaction, IN removes two 3′ nucleotides from each strand of the linear viral DNA, resulting in overhanging CA ends. In the second step, called strand transfer reaction, the newly formed 3′ OH act as nucleophilic agents and attack phosphoester bonds on the opposite strands of the target DNA (Brown, 1997). Recombinant HIV-1 IN, produced in *Escherichia coli*, can carry out both reactions in vitro in the presence of divalent ions such as Mg^{2+} and Mn^{2+} (Bushman and Craigie, 1991). In the same environment, it can also carry out the disintegration reaction that is the apparent reversal of the transfer step if presented with a synthetic dumbbell-shaped oligonucleotide (Chow et al., 1992).

Three distinct regions have been identified in the HIV-1 IN (288 residues) (Andrake and Skalka, 1996). The N-terminal domain, residues 1–49, contains a conserved HHCC motif that binds zinc in a 1:1 stoichiometry (Zheng et al., 1996). Zinc binding is believed to stimulate the multimerization process that enhances the activity (Lee et al., 1997; Deprez et al., 2000). The central catalytic core domain, residues 50–212, contains the catalytic site characterized by the essential D,D(35)E motif (D64, D116, and E152). Although all three domains are strictly required for processing and strand-transfer reactions, the core domain by itself can catalyze the disintegration step. The C-terminal domain, residues 212–288, contributes to DNA binding in a nonspecific manner and to the oligomerization that is necessary for the integration process (Brown, 1997). The 3D structure of each of the three domains is known at the atomic level. In the absence of structural data on the entire protein, the knowledge of the core domain structure and dynamics remains essential for inhibitor studies by docking techniques. Several x-ray crystallographic structures for the soluble catalytic core containing a mutation at the F185 position in the absence of divalent ions are now known. In the first available complete structure, a flexible loop 139–153 dangled out of the protein (Bujacz et al., 1996). The next structures were more compact (Maignan et al., 1998; Goldgur et al., 1998) and did not change much when the crystal was soaked with divalent ions. The structure of the catalytic core in the crystal of the bidomain sequence 52–288 is hardly modified (Chen et al., 2000).

The dynamics of the HIV-1 IN catalytic core has been simulated in the absence or presence of Mg^{2+} from a crystal structure lacking the flexible loop (Weber et al., 1998; Lins et al., 1999). The flexible loop was then built by analogy with homologous sequence in Rous sarcoma virus. The dynamics simulations of the entire hydrated catalytic core showed that the flexible loop retains some secondary structure. The binding of a second divalent ion does not decrease the flexibility in the region of residues 140–149 (Lins et al., 2000a). The second metal ion is likely to be carried into the HIV-1 IN active site by a DNA strand (Lins et al., 2000b).

In this work, two MD simulations were performed, one in the absence and the other in the presence of the physiological cation Mg^{2+}. The starting structures were taken as they can be found in the literature. Fluorescence properties were then deduced from the MD simulations and compared with experimental data.

MATERIALS AND METHODS

(50–212) Catalytic core domain preparation

pET-15b IN^{50-212}F185K expression vector encoding amino acids 50–212 of mutant soluble HIV-1 IN was generously donated by R. Craigie (Laboratory of Molecular Biology, NIDDK, NIH, Bethesda, MD). His-tagged IN catalytic core protein was overexpressed in *E. coli* BL21 (DE3) and purified under native conditions essentially as previously described (Jenkins et al., 1996). Briefly, at OD 0.8, bacterial cultures were induced by 1 mM isopropyl beta-D-thiogalactopyranoside and incubated for three hours at 37°C. The cell pellets were resuspended in ice-cold buffer A (20 mM Tris-HCl pH 8, 0.5 M NaCl, 4 mM β-mercaptoethanol, 5 mM Imidazol), treated with lysosyme for one hour on ice and sonicated. After centrifugation (30 min, 8000 × *g*), supernatant was filtered (0.45 μm) and incubated for at least 2 h with 1 ml of Ni-NTA agarose beads (Amersham Pharmacia Biotech, Umea, Sweden). The beads were washed twice with 10 volumes of buffer A, 10 volumes of buffer A + 50 mM imidazol, and 10 volumes of buffer A + 100 mM imidazol. His-tagged proteins were then eluted with buffer A + 1 M imidazol. The proteins were dialyzed overnight against 20 mM Tris-HCl pH 8, 0.5 M NaCl, 4 mM β-mercaptoethanol, and 10% glycerol (v/v). Aliquots were rapidly frozen on dry ice and stored at −80°C.

DNA substrates

Oligonucleotide DHIV $^{5'}$TGCTAGTTCTAGCAGGCCCTTGGGCCGGCGCTTGCGCC$_{3'}$ was purchased from Eurogentec (Liege, Belgium) and further purified on 18% acrylamid denaturing gel. For disintegration assays, 100 pmol of DHIV oligonucleotide was radiolabeled using T4 polynucleotide kinase (New England BioLabs (UK) Ltd., Hitchin, UK) and 50 μCi of [γ-^{32}P]ATP (3000 Ci/mmol). Kinase was heat-inactivated, and unincorporated nucleotides were removed by a passage through Sephadex G-10 column (Clontech Laboratories UK, Ltd., Hampshire, UK). NaCl was added to the final concentration of 0.1 M. Radiolabeled oligonucleotides were heated to 90°C for 2 min, and the DNA was annealed by slow cooling to room temperature.

Enzymatic disintegration assays

Disintegration assays were performed in the presence of 0.5 pmol of DHIV and 2 pmol of HIV purified catalytic core respectively (Leh et al., 2000). Enzymatic reactions were incubated at 37°C for 1 h. Products were separated in 15% denaturing polyacrylamid gel and analyzed using a STORM Molecular Dynamics phosphorimager.

Time-resolved fluorescence measurements

The time-resolved emission anisotropy was obtained by recording the two polarized emission decays Ivv(t) and Ivh(t), using the time-correlated single photon counting technique. The excitation light pulse source was a Ti-sapphire subpicosecond laser (Tsunami, Spectra Physics, Mountain View, CA) associated with a third harmonic generator tuned at 299 nm. The repetition of the laser was set down to 4 MHz. The fluorescence emission was detected through a monochromator (SpectraPro 150, ARC) set at 350 nm ($\Delta\lambda = 15$ nm) and a time-correlated single-photon counting card SPC-430 (Becker-Hickl GmbH, Berlin, Germany) was used for the acquisition of both excitation light pulse and fluorescence emission. The function of the instrumental response of the laser pulse (100 ps) was recorded by detecting the light scattered by a water solution. The time scaling was 11 ps per channel and 4096 channels were used. The two polarized components of the fluorescence decay and the instrumental response profile were alternatively collected during 90 and 30 s, respectively, until the total count of the Ivv component reached 22–26 millions (to insure a single-photon counting condition, the counting rate never exceeded 40 kHz). The correction for the monochromator transmission (G-factor = Ivv/Ivh) was determined from *N*-acetyl-tryptophanamide polarized decays under the same conditions. The microcuvette (volume 50 μl) was thermostated with a Haake type-F3 circulating bath. The catalytic core concentration was 500 nM in a buffer containing 20 mM Tris-HCl (pH 7.2), 0.1% NP-40 (v/v), 150 mM NaCl, 1 mM DTT supplemented with either 10 mM $MgCl_2$ or 1 mM EDTA. The anisotropy decay parameters were extracted from both parallel Ivv(t) and perpendicular Ivh(t) polarized fluorescence decay components elicited by vertically polarized excitation. The corresponding analysis was performed by the Quantified Maximum Entropy Method (MEM) (Brochon, 1994; Livesey and Brochon, 1987). This gave the distributions $h_f(\tau)$ for the fluorescence intensity decay and $h_a(\tau_c)$ for the anisotropy decay shown on Fig. 3 and 4. The experimental intensity decays shown on Fig. 11 were calculated using

$$I_e(t) = \sum_{\tau}(h_f(\tau)\exp(-t/\tau)) \Big/ \sum_{\tau} h_f(\tau). \tag{1}$$

The experimental anisotropy decays shown on Fig. 12 were calculated using

$$r_e(t) = r_e(0)\sum_{\tau_c}(h_a(\tau_c)\exp(-t/\tau_c)) \Big/ \sum_{\tau_c} h_a(\tau_c), \tag{2}$$

where $r_e(0)$ is the apparent experimental anisotropy at time 0.

Molecular dynamics

In all simulations, the catalytic core (residues 50–212) of the HIV-1 IN contained the single mutation F185H. The starting structure for the simulation of the dynamics in the presence of one Mg^{2+} ion was taken from the molecule C of the 1bl3 Brookhaven Protein Data Bank file (Maignan et al., 1998) for which the coordinates of all the residues of the catalytic loop are available. The end residues (210, 211, and 212) were added to the structure, which was then minimized using our quasi-Newtonian minimizer (Le Bret et al., 1991). Because the total charge of the protein with the Mg^{2+} cation is +1, one Cl^- counterion was added to make the elementary box electrically neutral. The 13 water molecules nearest to the Mg^{2+} cation were kept as they are in the PDB file. The starting structure for the simulation of the dynamics in the absence of Mg^{2+} ion was taken from the 2itg PDB file (Bujacz et al., 1996). Residues 50, 211, and 212 were added. In that case, an extra Na^+ cation was added in the simulation box. The system was embedded in a $50 \times 60 \times 50$ Å^3 box of water. The EDIT module of AMBER was modified so that a box of a given size could be filled with TIP3P water molecules having a density of 1 g/ml. For the simulations, there were 3835 (= 3822 + 13) and 3813 water molecules in the presence and in the absence of Mg^{2+} ion, respectively.

The SANDER module of AMBER (P. Kollman, University of California, San Francisco) was used to simulate the dynamics. The AMBER forcefield (Cornell et al., 1995) was complemented by the parameters of Mg^{2+}, Na^+, and Cl^- ions (Aqvist, 1990). Long-range Coulombic interactions were calculated using the particle-mesh technique (Darden et al., 1993) for Ewald sums (Ewald, 1921) with a cutoff of 10 Å and a grid size of $50 \times 60 \times 50$ Å^3. No correction was applied for the neglected long-range Van der Waals interactions because they are expected to be small. Covalent bonds containing a proton were constrained to their equilibrium length using the SHAKE algorithm (Ryckaert et al., 1977). The elementary integration time step was 2 fs. Before dynamics could be reliably produced, the system was prepared by two heating procedures. In the first procedure, only the water molecules were allowed to move, and the temperature was increased from 25 K to 300 K by 25 K steps during 14.6 ps. At the end of the first procedure, water molecules were cooled to 10 K. In a second procedure, the temperature of the whole system was increased from 10 K to 300 K over 18 ps. The velocities were then equilibrated during 13 ps at 300 K before dynamics production started. Frames were recorded at 0.1 ps interval.

Quantum mechanics

Quantum properties were calculated using the ab initio package Gaussian98 (Frisch et al., 1998). Indole, 3-methyl indole and 2-3 dimethyl indole were first optimized in the ground state at the restricted Hartree Fock level of theory using the basis $6-31+G(d)$. The ten first transitions of the optical spectrum were then computed using the CIS keyword (configuration interaction of single excited orbitals). Several n–π^* transitions were found. The first two π–π^* transitions were assigned to the ^1L_a and ^1L_b transitions.

FLUORESCENCE DECAYS SIMULATION

A proper simulation of fluorescence decays should follow step by step the detailed history of the protein from the absorption of a photon till the fluorescence emission. In the complete story (Callis, 1997), some events are easier to simulate than others. Our aim was to build a primitive model containing the elements that could be easily simulated. The simulation was then compared to the experimental data. Below, the simplifying hypotheses used to simulate the fluorescence properties of a protein after its dynamics are described:

1. Although all the aromatic residues of a protein are fluorescent, only the indole ring of Trp residues can absorb light when excitation wavelength is 299 nm. Throughout this work, the only absorbing or emitting species were the indole rings.
2. The intensity of the exciting laser beam used here was small enough so that single fluorescence photons were counted. At a given time, at most one Trp residue is assumed to be excited.
3. When the Trp residue is excited, the electronic distribution changes in about the same time as the time interval used here to integrate Newton law (2 fs). However, not all the conformations were recorded. The time interval separating two recorded successive conformations of the system was much longer (0.1 ps). Therefore, a residue was assumed either excited or lying in the ground state. In our simulation, the change occurred instantaneously. Once the chromophore is excited, the electrons are redistributed, which implies that the Coulombic charges, the bond, and valence angle parameters are modified. In a proper simulation, the force field of the excited chromophore should be modified. This concerns the equilib-

rium and rigidity values for each bond, each valence angle, each dihedral angle even, and the Coulombic charges. In this work, the chromophore was only virtually excited and kept in the simulation the same force field it had in the ground state. This hypothesis is not as natural as the previous ones and is only justified by the fact that MD simulations are, as they stand, time and disk demanding. We simply could not afford to generate a dynamics simulation where the force field changed according to the migration of the excitation.

4. The dynamics was simulated in a box that had a certain orientation relative to the laboratory. This would introduce privileged orientations because our simulation time was short relative to overall tumbling. We imagined that the same dynamics was replicated in all orientations relatively to the exciting laser beam.
5. The absorption spectrum was assumed to be the same for all Trp residues in the IN catalytic core whatever their position relatively to the solvent. This simplifying hypothesis is experimentally valid in the case of barnase (Willaert et al., 1992). Because of the last two hypotheses, each Trp residue had the same probability of absorbing light.
6. When a Trp residue absorbed light at time θ of the simulation, it had a certain probability p to be in the excited ^1L_a state and $(1 - p)$ to be in the excited ^1L_b state. When the excitation wavelength is 299 nm, p is certainly close to 1 (Valeur and Weber, 1977). However, the possibility that some of the residues may be excited in the ^1L_b state is worth studying. Besides, such a tool may be useful if the excitation wavelength is modified in future works. The absorbing transition moments $m_a(\theta)$ and $m_b(\theta)$ (in ^1L_a and ^1L_b states, respectively) were then computed from the coordinates of the Trp atoms and the ^1L_a or ^1L_b transition charges (see Table 1 and Fig. 1) according to

$$m(\theta) = \sum_{i} q_{i}^{*} r_{i}. \tag{3}$$

If the chromophore is excited to the ^1L_b state, it should return instantly to the ^1L_a state.

The fluorescence intensity that can be measured at $\theta + t$ when a chromophore absorbs light at θ, is proportional to the population that remains excited at $\theta + t$. Therefore the history of an excitation for the conformations between θ and $\theta + t$ needs to be followed and then averaged over θ. Here, four competing de-excitation pathways were considered.

De-excitation through emission of a photon

This occurs with a probability per time unit equal to the radiative rate constant, which is the inverse of the radiative lifetime $1/\tau_{rad}$. The Einstein fundamental relationship between the transition probabilities for induced absorption and emission and that for spontaneous emission has been modified, for a strongly allowed transition, to take into account the width of the absorbing band (Strickler and Berg, 1962). The radiative lifetime depends on the refraction index of the surrounding medium, the absorption, and the emission spectra of the chromophore. In contrast to the absorption spectrum, that can be assumed independent from the environment, the wavelength of maximum emission intensity is directly related with the electric field over the indole ring (Callis and Burgess, 1997). Because we have no experimental data on the wavelength of maximum emission intensity for each Trp residue in HIV-1 IN catalytic core, the radiative lifetime was considered as a parameter to be fitted.

TABLE 1 Trp Mulliken transition charges for ^1L_a and ^1L_b transitions

Tryptophan Atoms	^1L_a	^1L_b
N	0.0000	0.0000
H	0.0000	0.0000
CA	0.0203	−0.0008
HA	0.0000	0.0000
CB	−0.0725	0.0077
HB2	0.0004	−0.0006
HB3	0.0004	−0.0006
CG	0.0989	0.2954
CD1	−0.2700	−0.2486
HD1	−0.0127	−0.0091
NE1	0.0269	0.0480
HE1	−0.0056	−0.0008
CE2	0.4052	0.2758
CZ2	−0.6005	0.1105
HZ2	−0.0090	0.0133
CH2	0.6446	−0.0284
HH2	0.0188	0.0082
CZ3	−0.6050	0.1066
HZ3	−0.0029	0.0072
CE3	0.6166	−0.3580
HE3	0.0225	−0.0018
CD2	−0.2763	−0.2242
C	0.0000	0.0000
O	0.0000	0.0000

The transition charges are taken from 3-methylindole as given by the Gaussian98 program at the CIS/6-31+$G(d)$ approximation (see Materials and Methods). The charge of the in-plane hydrogen of the methyl group in 3 of 3-methylindole has been attributed to the Trp CA carbon atom.

De-excitation through proton transfers

A list of the amino acids that can donate a proton to the excited Trp residue is now available (Chen and Barkley, 1998). In this work, only the best donating groups were considered. The transfer was assumed to be possible if the Trp carbon atoms that receive the proton (CD1, CE3, and CZ2) (see Fig. 1) move into the immediate vicinity of the protons of the tyrosine hydroxyl, the cysteine sulfhydryl and the proton at the nitrogen delta of histidine. Because, in our HIV-1 IN catalytic core MD, these distances were never less

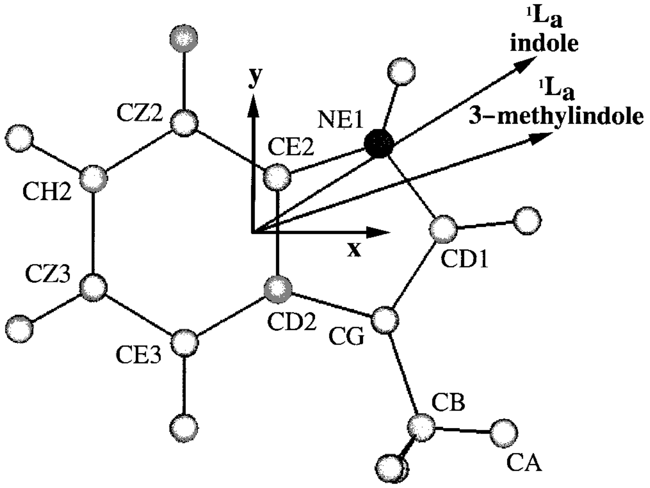

FIGURE 1 Optimized ground state geometry of the 3-methylindole with Trp atoms nomenclature. Trp CA carbon atom takes the place of the in-plane hydrogen of the methyl group in 3 of 3-methylindole. The ^1L_a transition moments $\langle\Psi_{\text{ground}}|er|\Psi_{\text{excited}}\rangle$ for indole and 3-methylindole are drawn as given by the ab initio program Gaussian98 (see Materials and Methods). A small error is introduced in the direction of the transition moments when, in a first step, the Mulliken transition electron distribution is centered on the nuclei as shown on Table 1 and, in a second step, Eq. 3 is used. The moment (not drawn for clarity) lies 10° from the 3-methylindole moment and 4° from the indole moment. The x and y axes mentioned in Table 1 are drawn.

than 3 Å (data not shown), de-excitation through proton transfer was assumed to be inefficient.

De-excitation through emission of an electron

Among the many possible quenching processes (Chen and Barkley, 1998), only the quenching by the peptide bond (Chen et al., 1996) was taken into account using the formula derived by Marcus and Sutin (1995) as recently modified (Sillen et al., 2000). The instantaneous lifetime τ_i of the Trp residue i, was assumed to be modulated only by the distance r (Å) of its CE3 atom to the closest C carbon atom of the peptide bond along the chain to which it belongs,

$$\tau_i^{-1} = \tau_{\text{rad}}^{-1} + k_0 \exp(-\beta(r-3)). \tag{4}$$

In this formula, k_0 and β are parameters to be fitted.

De-excitation through fluorescence resonance energy transfer

In the last de-excitation pathway, the excitation migrates due to Trp–Trp homotransfers. The rate of fluorescence resonance energy transfer that occurs from the donor D to the acceptor A is given by

$$k_{D\to A} = \frac{3}{2}\frac{R_0^6}{\tau_D}G^2. \tag{5}$$

In this classical formula (Förster, 1948), τ_D is the lifetime of the donor. G is defined through a multipolar expression (Le Bret et al., 1977),

$$G = \frac{1}{m_A m_D}\sum_{i\epsilon A}\sum_{j\epsilon D}\frac{q_i^* q_j^*}{r_{ij}}, \tag{6}$$

where m_A and m_D are the ^1L_a transition moments of the acceptor and the donor, q_i^* and q_j^* are the ^1L_a transition charges of the acceptor and of the donor, respectively (see Table 1), and r_{ij} is the distance separating the donor atoms from the acceptor atoms. When the distance between the centers of the donor and the acceptor (r_{DA}) is large, the multipolar function G reduces to a purely geometric factor G_∞ that is traditionnally written as

$$G_\infty = \kappa/r_{DA}^3, \tag{7}$$

where the so-called orientation factor κ is defined from the unit vectors along the transition moments (μ_A and μ_B) and the unit vector of the line connecting the donor and acceptor centers (u),

$$\kappa = \mu_A \cdot \mu_D - 3(u\cdot\mu_A)(u\cdot\mu_D). \tag{8}$$

G depends on the geometry of a pair of chromophores, regardless of which is the donor, and which is the acceptor. Table 2 shows the ratio of $(G_\infty/G)^2$ when two superposed Trp residues are translated along the three axes as defined in Fig. 1. For example, an error of 20% was observed when the Trp residues were translated along y even if the chromophores were separated by 30 Å, which is considered a long distance. The relative error could be very large when either G or G_∞ was close to zero because of its orientation. The relative error was much less when the two chromophores were first translated and then randomly rotated about their centers (Table 2).

TABLE 2 Förster transfer rate between two Trp residues in their ^1L_a states

r_{DA} (Å)	Translation			Translation and Random Rotation ($\kappa^2 = 0.667$)
	Along x Axis ($\kappa^2 = 2.030$)	Along y Axis ($\kappa^2 = 0.183$)	Along z Axis ($\kappa^2 = 0.994$)	
10	0.6656	76.37	1.236	0.7076
20	0.8681	1.578	1.064	0.9317
30	0.9357	1.195	1.029	0.9744
40	0.9626	1.101	1.016	0.9866
50	0.9757	1.062	1.011	0.9899

Two Trp residues were superposed, then translated by r_{DA} (Column 1) along one of the three axes shown on Fig. 1 (Columns 2–4). In the last column, the orientations of the translation and of the residues are randomized. The orientation factor κ (Eq. 8) is indicated in the third row. In each case, the Table shows the ratio of dipolar to multipolar approximations $(G_\infty/G)^2$.

In Eq. 5, the transfer rate $k_{D\rightarrow A}$, is also characterized by the distance R_0,

$$R_0^6 = \frac{2}{3} \times \left(\frac{9 \ln 10}{128\pi^5 N_{av}}\right)\frac{\phi_D}{n^4}\int_0^\infty F_D(\lambda)\varepsilon_A(\lambda)\lambda^4\, d\lambda, \quad (9)$$

where the expression between parentheses is a pure number equal to 8.79×10^{-28}, N_{av} is the Avogadro number, ϕ_D is the fluorescence quantum yield of the donor, n is the refractive index of the medium separating the donor from the acceptor, $F_D(\lambda)$ is the normalized emission spectrum of the donor ($\int_0^\infty F_D(\lambda)\, d\lambda = 1$), and $\varepsilon_A(\lambda)$ is the molar absorption coefficient of the acceptor. From Eq. 5 and 9, the transfer rate depends on both the absorption spectrum and the ratio ϕ_D/τ_D, which is the inverse of the radiative lifetime of the donor. It is convenient to group all parameters that depend on spectral properties in a single parameter $S_{D\rightarrow A}$ (Å^6/ns) so that the Förster formula reads

$$k_{D\rightarrow A} = S_{D\rightarrow A}G^2. \quad (10)$$

The spectral parameter $S_{D\rightarrow A}$ depends on the radiative lifetime and on the overlap between the donor emission and acceptor absorption spectra. Here, the absorption spectrum is assumed to be independent of the solvent accessibility. In contrast, when the residue is fully exposed to the aqueous medium, the emission spectrum is assumed to be shifted to the red and does not overlap well the absorption spectrum. As a consequence, the transfer rates k_{ij} and k_{ji} differ through the spectral parameter $S_{D\rightarrow A}$ if the environment of residues i and j differ.

Computation of the fluorescence intensity decay

The fluorescence intensity at time t is proportional to the amount of chromophores that are still excited, at time t, after absorption. Therefore, the populations X_i ($i = 1, \ldots, N$) of excited residues must be kept track of frame after frame. Here, N, is the number of Trp residues and is either 4 or 8 according to the monomeric or dimeric state of the IN catalytic core. The frames were recorded at time interval δ (namely 0.1 ps). The conformation of the protein is assumed to be the same between times $\theta' - \delta/2$ and $\theta' + \delta/2$. In that case, the populations X_i follow a system of N linear equations,

$$\frac{dX_i}{dt} = \sum_j K_{ij}X_j. \quad (11)$$

When i and j differ, K_{ij} is exactly the resonance energy transfer rate k_{ij} from the donor j to the acceptor i. The diagonal terms depend on the instantaneous fluorescent lifetimes and the sum of resonance energy transfer rates from i to j,

$$K_{ii} = -1/\tau_i - \sum_{j\neq i} k_{ij}. \quad (12)$$

Because the matrix K is assumed to be constant during $\theta' - \delta/2$ and $\theta' + \delta/2$, setting (see Appendix),

$$M(\theta') = \exp(K\delta/2), \quad (13)$$

we have

$$X(\theta' + \delta/2) = M^2(\theta') \cdot X(\theta' - \delta/2). \quad (14)$$

The computations should be done on N vectors X, each of them corresponding to a different absorbing chromophore. It is convenient to introduce an $N \times N$ matrix, F, to perform all the computations simultaneously. The population of excited residue i at $\theta + t$, $t = n\delta$ when j has been excited at θ, is the element F_{ij} of the matrix $F(\theta, \theta + n\delta)$. Because each of the N Trp residues has the same probability of absorbing, the matrix $F(\theta, \theta)$ is a scalar matrix with diagonal elements equal to $1/N$. $F(\theta, \theta + n\delta)$ is obtained by successive multiplications,

$$F(\theta, \theta + n\delta) = M(\theta + n\delta) \cdot M(\theta + (n-1)\delta) \cdot F(\theta + (n-1)\delta). \quad (15)$$

Finally the simulated fluorescence intensity $I(t)$ is the sum of all elements of the average over θ of the matrix $F(\theta, \theta + t)$,

$$I(t) = \left\langle \sum_{i,j} F_{ij}(\theta, \theta + t) \right\rangle. \quad (16)$$

The brackets $\langle\,\rangle$ call for the averaging over θ. If the total number of frames is L, the averaging for n takes into account $L - n$ values. Therefore, the decay points are the average of more values and are more accurate for smaller values of t (or of n). The decay (Eq. 16) has to be compared to the experimental one, corrected from the shape of the flash, $I_e(t)$ (Eq. 1).

Simulation of the anisotropy decay

The anisotropy at time t is computed as follows:

$$r(t) = r_0\left\langle \sum_{i,j} F_{ij}(\theta, \theta + t)\left[\frac{p(3(\mu_{ai}(\theta) \cdot \mu_{aj}(\theta + t))^2 - 1)}{2} + \frac{(1-p)(3(\mu_{bi}(\theta) \cdot \mu_{aj}(\theta + t))^2 - 1)}{2}\right]\right\rangle. \quad (17)$$

In this formula, the Trp residues i, are supposed to be excited at time θ with probability p in their ^1L_a band (unit transition moment μ_a) and with the probability $(1 - p)$ in their ^1L_b band (unit transition moment μ_b). All residues j emit from their ^1L_a band at time $\theta + t$. As above, $F_{ij}(\theta, \theta + t)$ is the probability that j is still excited at time $\theta + t$ when i was excited at time θ. The expression between brackets $\langle\,\rangle$ is averaged over the values of θ. It is more accurate for smaller values of t. r_0 is the fundamental anisotropy. The calculated anisotropy decay (Eq. 17) has to be compared to the experimental one, $r_e(t)$ (Eq. 2).

RESULTS

Enzymatic activity

Recently, we prepared an entire HIV-1 IN that catalyzes 3′ processing, strand transfer and disintegration reactions in the presence of the likely physiological cation, Mg^{2+} (Leh et al., 2000). The (50–212) core domain of IN was purified in the same condition (i.e., in absence of detergent) and assayed for its activity on a dumbbell-shaped DNA substrate. The activity of the protein was followed by the appearance of a short 14-mer oligonucleotide cleaved from the 38-mer DNA substrate (Chow et al., 1992). Results of this assay in the presence of either Mn^{2+} or Mg^{2+} at increasing temperature are shown in Fig. 2. The (50–212) truncated protein efficiently performed the disintegration reaction using a dumbbell substrate, although it was active only when Mn^{2+}, but not Mg^{2+}, was present. Although some disintegration product could be detected after 60 mn at 4°C, the reaction yield showed a constant increase over the temperature range reaching a maximum at 37°C.

Experimental fluorescence decays

The fluorescence intensity and anisotropy decays of the IN catalytic core have been measured in the presence of either Mg^{2+} or the chelating agent EDTA at both 5°C and 30°C. The decays can be decomposed into a distribution of exponentials as shown in Fig. 3 (at 5°C) and Fig. 4 (30°C). There was small effect of the divalent cation on both intensity and anisotropy decays. Temperature also had little effect on the intensity decays. In contrast, short correlation times (<3 ns) were drastically more populated at 30°C. The longest correlation time remained similar at both temperatures in the absence of Mg^{2+}, and was even slightly higher at 30°C than at 5°C in the presence of Mg^{2+}. This was unexpected because the longest correlation time can be interpreted as the rotational correlation time, τ_c of a rigid sphere of volume V. It depends on the solvent viscosity, η, the absolute temperature, T, and the Boltzman constant, k, according to the Perrin (1929) equation,

$$\tau_c = \eta V/kT. \tag{18}$$

For aqueous solutions, the ratio η/T decreases by a factor 2.065 from 5°C to 30°C. The experimental values at 5°C and 30°C of the long rotational correlation time suggested that the volume has doubled. The catalytic core would be monomeric at low temperatures and dimeric at 30°C (see discussion) at a temperature at which it is enzymatically active.

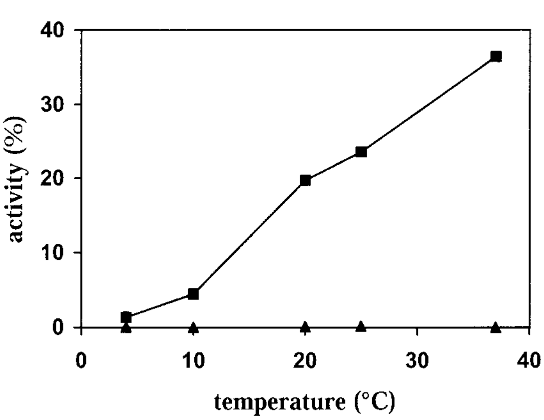

FIGURE 2 Disintegration activity of the HIV-1 IN catalytic core expressed as the percentage of product per dumbbell-shaped substrate as a function of temperature, in the presence of 10 mM Mn^{2+} (*squares*) and 10 mM Mg^{2+} (*triangles*).

Dynamics of the flexible loop

For each frame of both dynamics (with or without Mg^{2+}), the dihedral angles $\varphi_i = C_{i-1}\text{-}N_i\text{-}CA_i\text{-}C_i$ and $\psi_i = N_i\text{-}CA_i\text{-}C_i\text{-}N_{i+1}$ of the protein were compared with those of the starting structures φ_{i0} and ψ_{i0}. The $\varphi - \psi$ root-mean-squared deviation (RMSD) was calculated at each time of the simulation using

$$\varphi - \psi\mathrm{RMSD} = \left(\frac{\sum_{i=n_1,n_2} (\varphi_i - \varphi_{i0})^2 + (\psi_i - \psi_{i0})^2}{2(n_2 - n_1 + 1)} \right)^{1/2}. \tag{19}$$

$\varphi - \psi$RMSD from residue $n_1 = 51$ to residue $n_2 = 211$ are plotted in Fig. 5. After a half-nanosecond transient evolution, both the $\varphi - \psi$RMSD reached a plateau showing that the dynamics are stable. If the same analysis was done on the loop (from $n_1 = 139$ to $n_2 = 153$), the $\varphi - \psi$RMSD was slightly larger (Fig. 6). Moreover, in the absence of Mg^{2+}, a second transition was observed around 3.4 ns (Fig. 6 *A*) where the $\varphi - \psi$RMSD increased from 60 to 80° and seemed to drop down toward the end of the simulation. In the presence of cation, $\varphi - \psi$RMSD was smaller and retained a value around 50° (Fig. 6 *B*).

Whether a residue is part of a helix can be determined for each frame of the simulation using the DSSP program (Kabsch and Sander, 1983). Most residues remained part of the same structure throughout the simulation. The flexible loop (139–153) had unique behavior in this respect. The end of the flexible loop can take on the structure of the adjacent α4 helix, which, at its largest extension, comprises residues 147 to 168 in crystal structures. In the absence of cation, no structure was observed in our simulation before 3.4 ns (Fig. 7 *A*). After that time, the α4 helix extended transitorily down to residue 151 (Fig. 7 *A*). In the presence of cation, the α4 helix extended permanently till V150, and,

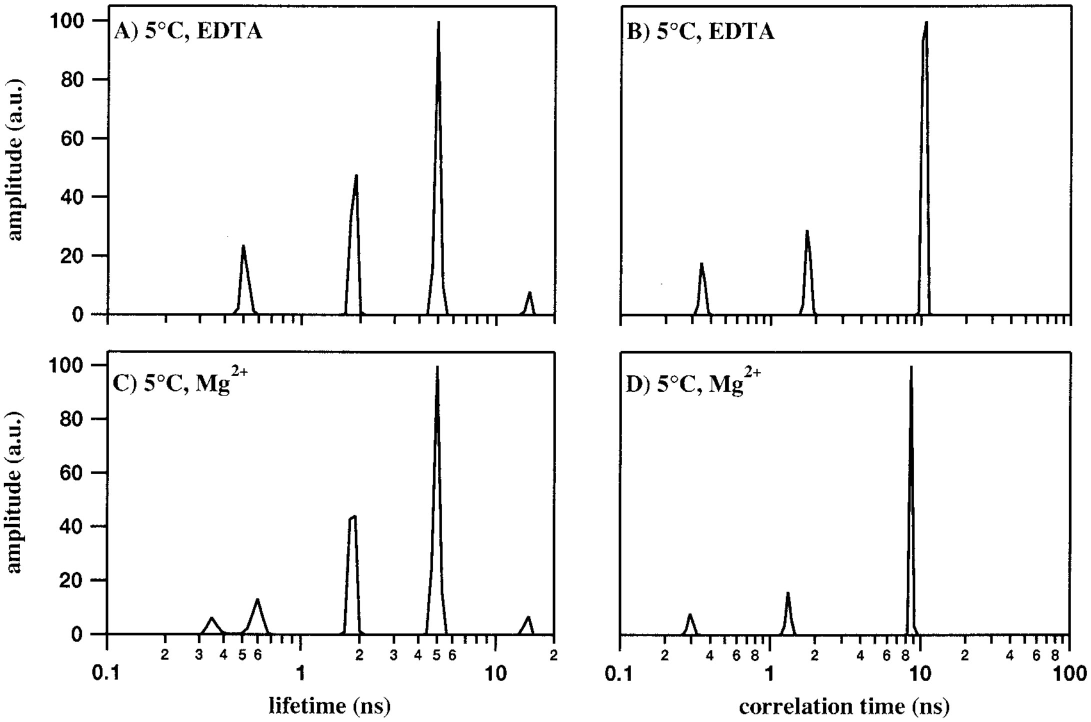

FIGURE 3 Experimental determination of the HIV-1 IN catalytic core lifetimes and correlation times at 5°C. (*A*) and (*C*) Lifetimes distributions. (*B*) and (*D*) Correlation times distributions. The distributions were recovered by the Quantified Maximum Entropy Method as indicated in Materials and Methods: (*A*) and (*B*), in the presence of 1 mM EDTA, (*C*) and (*D*) in the presence of 10 mM Mg^{2+}.

as a transient feature, till P145 (Fig. 7 *B*). The rest of the loop (144–139) was always disordered.

Because it is supposed to play a key role in the catalytic activity of the enzyme, the conformation of the D,D(35)E motif has been thoroughly studied. In the first complete crystallographic structure, the oxygen atoms of E152 pointed away from those of D64 and D116 (Bujacz et al., 1996), in contrast with the conformation they had in another cognate system, the avian sarcoma virus catalytic domain (Bujacz et al., 1995). A synthetic way to monitor the relative oxygen conformation is to compute the interaction energy of E152 distal oxygen atoms and D64 and D116. This interaction is the sum of the electrostatic and Van der Waals contributions to the energy. It increases when the oxygen atoms are closer. In the presence of Mg^{2+}, the oxygen atoms were in the expected conformation from the very beginning (Fig. 8 *B*). In contrast, in the absence of Mg^{2+}, the E152 distal oxygen atoms pointed away. However, after 3.4 ns, the oxygen atoms became spontaneously closer (Fig. 8 *A*). This conformational change occurred simultaneously with the $\varphi - \psi$RMSD transition as shown in Fig. 6 *A*.

Dynamics of tryptophan residues

Because of our interest for fluorescence simulation, some important parameters concerning the Trp residues have been computed. To estimate the number of water molecules close to the Trp residues, the following function was computed,

$$f = \sum_{i_{\mathrm{Trp}}-j_{\mathrm{water}}} r_{ij}^{-6}, \tag{20}$$

where the index i runs over the indole atoms and j runs over the water molecule oxygen atoms. It becomes larger when there are more water molecules and when the latter are closer to the Trp residue. Such a function reflects the induced dipole contribution to the Van der Waals interactions between the Trp residue and the water molecules. It was preferred over counting the water molecules, because counting the molecules depends on an arbitrarily chosen cut-off value. From inspection of the conformations using visualization systems, a value of f about 0.07 corresponds to a Trp residue completely exposed to water. The average value of f and its fluctuation over time are reported for each residue in Table 3. Therefore, during both dynamics, in presence and in absence of Mg^{2+}, W131 and W132 were completely exposed to water, W108 was half exposed, and W61 was buried. Therefore, when simulating energy-transfer rates, the fully solvent exposed chromophores, W131 and W132, were treated as poor donors, whereas the less exposed chromophores, W61 and W108, were treated as good donors. Moreover, Table 3 shows in which secondary structure the Trp residues were involved. All four Trp

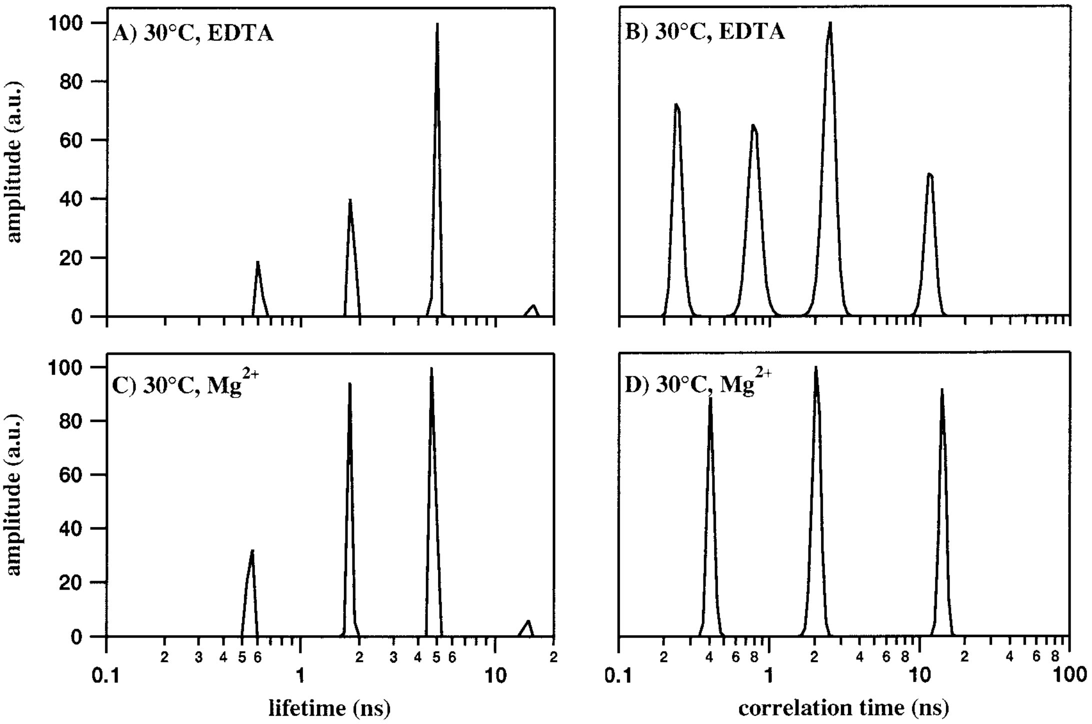

FIGURE 4 Experimental determination of the HIV-1 IN catalytic core lifetimes and correlation times at 30°C. (*A*) and (*C*) Lifetimes distributions. (*B*) and (*D*) Correlation times distributions. The distributions were recovered by the Quantified Maximum Entropy Method as indicated in Materials and Methods: (*A*) and (*B*) in the presence of 1 mM EDTA, (*C*) and (*D*) in the presence of 10 mM Mg^{2+}.

belonged to the same secondary structure during the MD. Figure 9 shows the evolution of the dihedral angles χ_A = C-CA-CB-CG and χ_B = CA-CB-CG-CD1 (see Fig. 1 for atom nomenclature) for the Trp side chains in the presence and absence of cation. Both dihedrals of W61 and W108 kept the same values throughout the simulations in contrast with those of W131 and W132.

Dipolar versus multipolar approximation

The evolution of the instantaneous values of the parameter *G* is shown on Fig. 10 for each Trp–Trp pair along the MD trajectories in the absence of Mg^{2+}. The multipolar approximation (above the diagonal) can be easily compared to the dipolar approximation (under the diagonal). Results were similar in the presence of Mg^{2+} (data not shown). Although both approximations gave similar general trends in most conformations, in rare cases they could be completely different (see W61–W108 around 1 ns). This shows that the dipolar approximation is rather crude. Figure 10 also shows another interesting feature: *G* changed very rapidly. It could jump from a negative to a positive value within 0.1 ps (see W131–W132 around 4 ns). This implied that it passed through zero in the meantime. The amplitude of the jumps was not constant during the simulation. Most pairs endured several regimes (Fig. 10).

Fitting the intensity and anisotropy decays

The simulation assumes that the resonance transfer rates remain constant between two recorded conformations. This assumption is not valid as the geometric contribution *G* jumps from favorable to unfavorable orientations within two recorded frames. Then it becomes necessary to check that the results do not depend on what happens between two successive recorded conformations. Therefore, the dynamics were filled with 10 or 100 conformations chosen randomly among the closest 100 frames. The simulated fluorescence intensity and anisotropy decays were identical to the fourth significant digit (data not shown). Therefore, the rates can be assumed constant (although in actuality they are not).

According to our hypotheses, the fluorescence decay depends on few parameters: τ_{rad}, β, k_0, and $S_{D\rightarrow A}$ (see Eqs. 4 and 10). The values for these parameters may first be taken from the literature. The radiative lifetime may easily be estimated for Trp derivatives that have a mono exponential decay. Under these conditions, the radiative lifetime is the ratio of the measured lifetime to the quantum yield. For *N*-acetyltryptophanamide, τ_{rad} is 21.4 ns, and, for *N*-acetyltryptophan, it is 22.9 ns (Szabo and Rayner, 1980). More recently, an empirical relationship between the radiative lifetime and the wavelength of maximum emission intensity

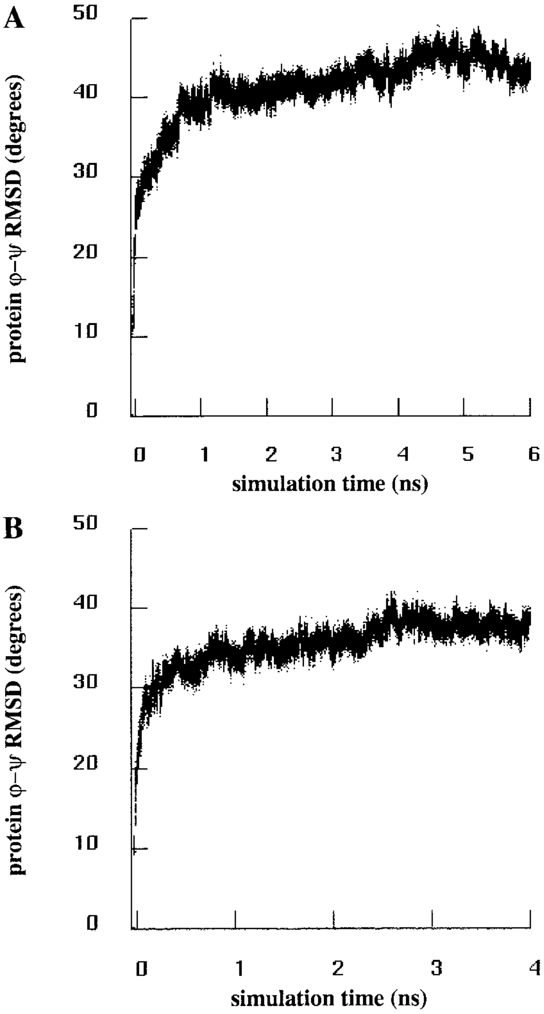

FIGURE 5 $\varphi - \psi$RMSD for all residues of the HIV-1 IN catalytic core during the MD. (*A*), In the absence of divalent cation. (*B*), In the presence of Mg^{2+}.

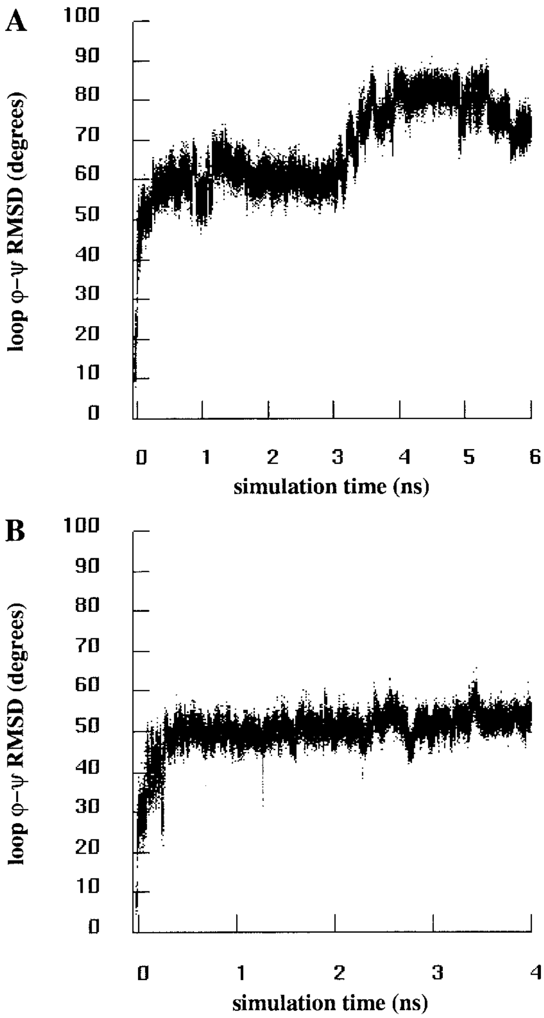

FIGURE 6 $\varphi - \psi$RMSD for residues 139–153 of the HIV-1 IN catalytic core during the MD. (*A*) In the absence of divalent cation. (*B*) In the presence of Mg^{2+}.

λ_{max} was proposed (Sillen et al., 2000): τ_{rad} varies from 18.2 ns to 23.5 ns when λ_{max} varies from 320 to 345 nm. In the absence of experimental data, τ_{rad} was first uniformly set equal to 20 ns for all four chromophores. Sillen et al. (2000) propose for β, 1.9 $Å^{-1}$, and for k_0, the electron transfer rate from the surface of Trp, 25 ns^{-1}. Studies on barnase show that the values of $S_{D \rightarrow A}$ depend on the environment of the donor (Willaert et al., 1992). Because they are surrounded by water, W131 and W132 are bad donors and their $S_{D \rightarrow A}$ was set to 133,000 $Å^6$/ns. W61 and W108 are considered as good donors and their $S_{D \rightarrow A}$ was set to 641,000 $Å^6$/ns. This set of values gave a steeper fluorescence intensity decay both in the absence (Fig. 11 *A*, *curve 3*) and in the presence of divalent cation (Fig. 11 *B*, *curve 3*) when compared with the experimental curves obtained at the two different temperatures 5°C and 30°C (*curves 1* and *2*).

To fit the experimental 6-ns fluorescence decay in the absence of cation at 5°C, the electron transfer rate constant k_0 must be set ~3.7 ns^{-1} and the values of the parameters $S_{D \rightarrow A}$ divided by 100 (Fig. 11 *A*, *curve 4*). In the presence of Mg^{2+}, the best fit to the 4-ns decay was obtained when k_0 was set ~4.6 ns^{-1}, and again the values of the parameters $S_{D \rightarrow A}$ should be divided by 100 (Fig. 11 *B*, *curve 4*). At 30°C, a good fit was obtained with k_0 set ~3.1 and 5.2 ns^{-1} in the absence and in the presence of Mg^{2+}, respectively (data not shown). A change of τ_{rad} from either 20–22 or 25 ns had no influence on the results (data not shown). Figure 11 also shows simulated decays with β set to 1.7 and 2.1 $Å^{-1}$ (*curves 5* and *6*). Clearly, in all cases, the best fit values for β, ~1.9 $Å^{-1}$, agreed with Sillen et al. (2000). Apparently, the values of τ_{rad} and β, to a lesser degree, are not so critical as that k_0. Typically, the best-fitting simulated decays are too slow in the first 200 ps, then too rapid untill about 2 ns, then too slow later on. The optimal value of k_0 depends on the size of the window. If the data are analyzed within 200-ps windows, the electron transfer rate k_0 must be

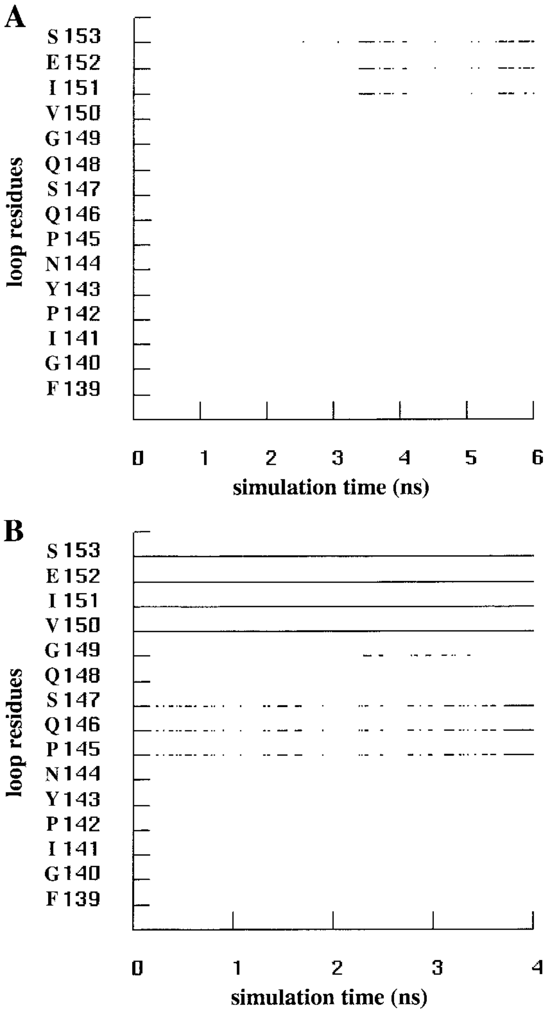

FIGURE 7 Time-dependent secondary structure analyses for the helicity of residues 139–153. A dot means that the residue belongs to an α helix as determined by the DSSP program. (*A*) In the absence of divalent cation. (*B*) In the presence of Mg^{2+}.

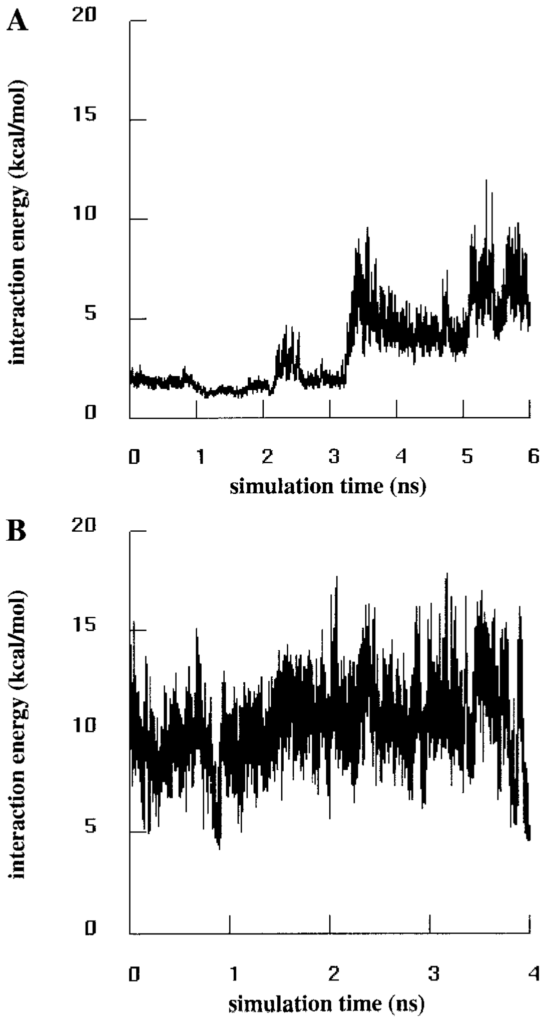

FIGURE 8 Interaction energy between the E152 distal oxygen atoms and those of D64 and D116 during the MD. (*A*) In the absence of divalent cation. (*B*) In the presence of Mg^{2+}.

increased to values ~27 ns^{-1} in closer agreement with the value reported by Sillen et al. (2000).

Once the intensity decay is fitted, the only parameters that can be modified for the anisotropy decay simulation are the population p of ^1L_a excited states and the fundamental anisotropy r_0. Now, for the excitation wavelength of 299 nm, the value of p is close to 1 (Valeur and Weber, 1977). The simulated anisotropy has a very steep drop between 0 and 0.1 ps, in a time that is much less than the time response of the apparatus. Therefore, the simulated point at $t = 0$ was skipped. The ^1L_a contribution of the simulated anisotropy at 0.1 ps was then scaled to the experimental point to give the curves shown on Fig. 12. The calculated anisotropy decay (Fig. 12, *curve 4*) obtained using optimized parameters as defined in Fig. 11, was compared to the experimental decays. Because the simulated decays are computed as time-correlation functions from the MD simulations, they are significant only at their beginning, at low values of t. For the 5°C experimental decay in the absence of cation (Fig. 12 *A*, *curve 1*), the fit was good. In the presence of cation, the simulated anisotropy was fitted in the same way. Only the fit during the first half-nanosecond was very satisfying (Fig. 12 *B*; compare *curves 1* and *4*). The simulated anisotropy decay could not be fitted to the 30°C experimental anisot-

TABLE 3 Hydration factor and secondary structure of HIV-1 catalytic core Trp residues

	Hydration Factor $f \times 10^{-3}$		Structure	
Residue	Without Mg^{2+}	With Mg^{2+}	Without Mg^{2+}	With Mg^{2+}
W61	1.4 ± 0.2	1.3 ± 0.1	91%, $\beta 2$ sheet	100%, $\beta 2$ sheet
W108	34.9 ± 11.3	22.6 ± 8.6	100%, coil	100%, coil
W131	74.9 ± 13.2	64.5 ± 21.9	100%, $\alpha 3$ helix	99%, $\alpha 3$ helix
W132	68.9 ± 11.9	61.3 ± 14.1	100%, $\alpha 3$ helix	97%, $\alpha 3$ helix

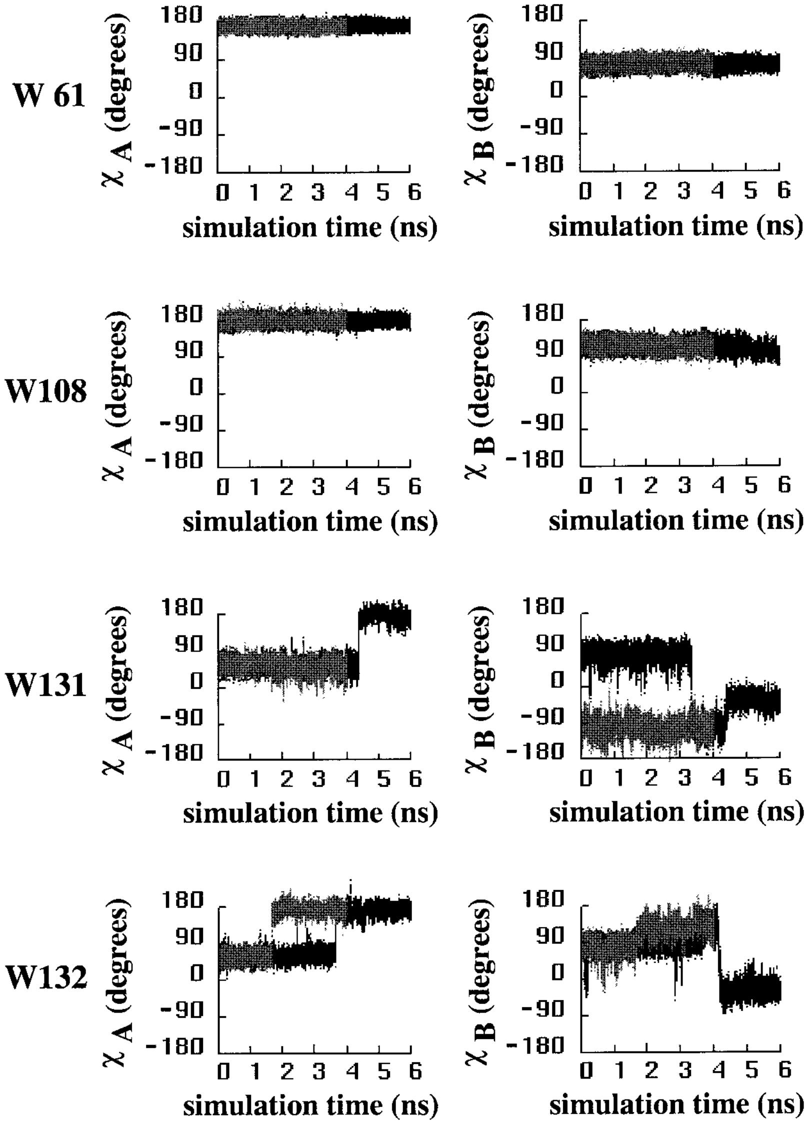

FIGURE 9 Evolution of the side chain dihedral angles χ_A = C-CA-CB-CG (*left column*) and χ_B = CA-CB-CG-CD1 (*right column*) for the four Trp residues during the MD. *Black dots*, in the absence of divalent cation. *Gray dots*, in the presence of Mg^{2+}. Because gray and black traces largely overlap, black dots are often hidden by gray dots.

ropy decay with similar parameters (Fig. 12, *curve 2*). The fit could be obtained if the spectral parameters were drastically increased: $S_{D \rightarrow A}$ should be set equal to 13,300 Å^6/ns for a poor donor and to 64,100 Å^6/ns for a good donor (curve not drawn on Fig. 12 for clarity).

As shown before, the catalytic core is probably dimeric at 30°C. It was then interesting to use the dynamics on the monomer unit of the catalytic core to build, at each frame, a chimeric dimer as it is in four crystal structures (Bujacz et al., 1996; Maignan et al., 1998; Goldgur et al., 1998; Chen et al., 2000). The transformation matrix was computed using the dimer crystal structure, then reported to a reference bound to monomer atoms. Due to the construction procedure, the global motion of the chimeric dimer in the simulation was the same as that of the monomeric unit. Therefore, the experimental anisotropy was recomputed using Eq. 2 with its longest correlation time divided by two. This did not change much in terms of the steepness of the experimental curve during the first nanosecond, the range we were interested in (Fig. 12, *curve 3*). In the chimeric dimer simulations, the system had 8 Trp residues, and W108 was very close to its image. However, the transfers were not sufficient to make the simulated anisotropy decay as fast as the 30°C experimental data with the values of $S_{D \rightarrow A}$ set to 1330 Å^6/ns and 6410 Å^6/ns.

DISCUSSION

In this paper, time-resolved fluorescence properties of HIV-1 IN catalytic core were studied. The experimental intensity decays depended little on Mg^{2+} binding or on temperature. In contrast, the anisotropy decays depended heavily on temperature. The longest correlation time is related to the global motion of the system. A spherical 18.7-kD protein with a 50% hydration volume is expected to

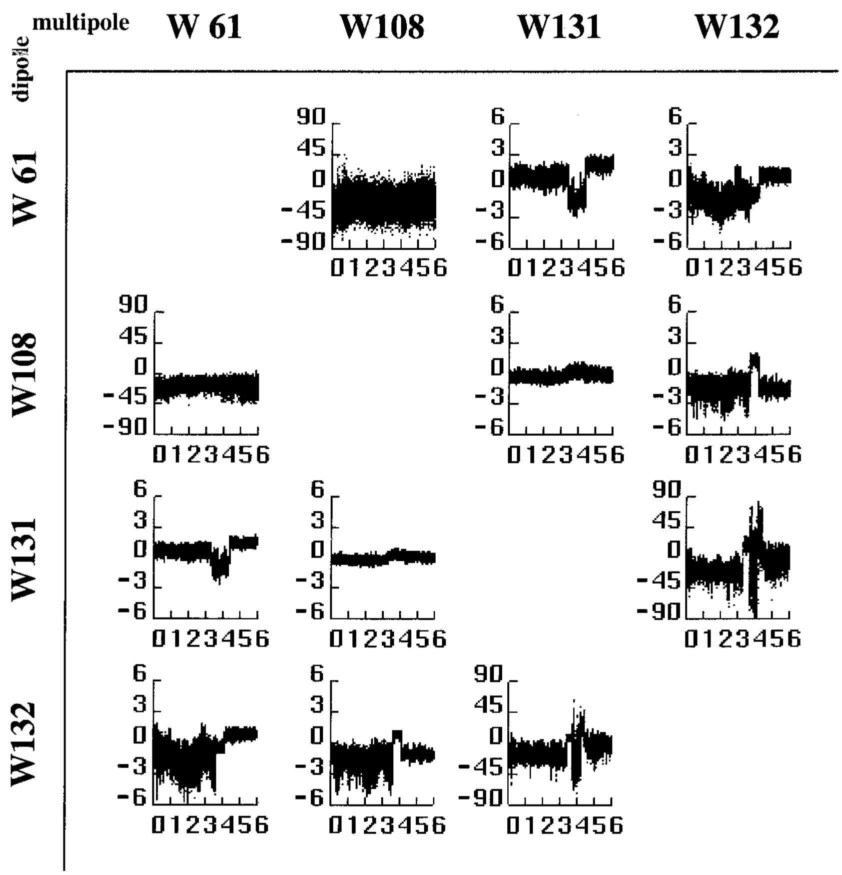

FIGURE 10 Time evolution (time unit:ns) of the dimensionless geometric contribution ($\times 10^4$) to the fluorescence resonance energy transfer rates for each Trp–Trp pair displayed in matrix outlay. *Above the diagonal*, multipolar approximation (G, Eq. 6). *Below the diagonal*, dipolar approximation (G_∞, Eq. 7).

have a correlation time of 13.5 ns at 5°C and 6.6 ns at 30°C in aqueous solutions. The experimental data for the HIV-1 IN catalytic core with or without Mg^{2+} agreed with the expected value at 5°C but not at 30°C. This could simply be explained by a dimerization of the catalytic core at 30°C. When the temperature was increased, we observed a drastic increase of the amplitudes of the shorter correlation times. This could have been caused by partial denaturation, and the activity of the catalytic core was then checked as a function of temperature. Because the catalytic core is inactive for either the 3′-processing or the integration reaction, the disintegration activity (Chow et al., 1992) was tested. Interestingly, the catalytic core was active only with manganese as a cofactor. This result has already been obtained with truncated proteins in which either the N-terminal or the C-terminal domain was deleted (Leh et al., 2000). In contrast, the entire IN was active in both Mg^{2+}- and Mn^{2+}-dependent disintegration (Leh et al., 2000). Why magnesium is not efficient in the disintegration reaction by the three different truncated IN proteins is a pending question for the present time. Nevertheless, the divalent cation-bound protein MD simulation was carried out with Mg^{2+} instead of Mn^{2+} for two main reasons: no structural data of HIV-1 IN are available in the presence of Mn^{2+}, and the Mg^{2+} cofactor is more relevant for the in vivo activity of the entire protein because it is maintained at higher concentration in the cytoplasm of living cells (about 10^{-3} M "free" Mg^{2+} versus 10^{-7} M Mn^{2+}).

In both MD simulations, the starting conformations were taken as they stand in literature without trying to make them look like any standard. In the absence of Mg^{2+}, the protein is very flexible and takes on several different conformations during the 6-ns simulation. We observed that the loop F139–S153 remained flexible except for the residues 151–153 that are transitorily part of the $\alpha 4$ helix. The residue E152 within the D,D(35)E motif, which is strictly required for the catalysis, had a natural tendency to orient itself to form what was assumed to be a correct active site. If we could have produced a much longer simulation we would have probably found the same loop conformation as those described in recent x-ray studies (Goldgur et al., 1998; Maignan et al., 1998) or dynamics (Weber et al., 1998; Lins et al., 1999). A stabilized, extended $\alpha 4$ helix could be observed after some 50 ns (Doniach and Eastman, 1999). The binding of Mg^{2+} drastically slowed down the rate of conformation changes so that the number of different conformations that were generated during 4 ns decreased. This does not contradict the flexibility that is experimentally observed as necessary for the activity: glycine residues G140 and G149, that appear to act as conformational

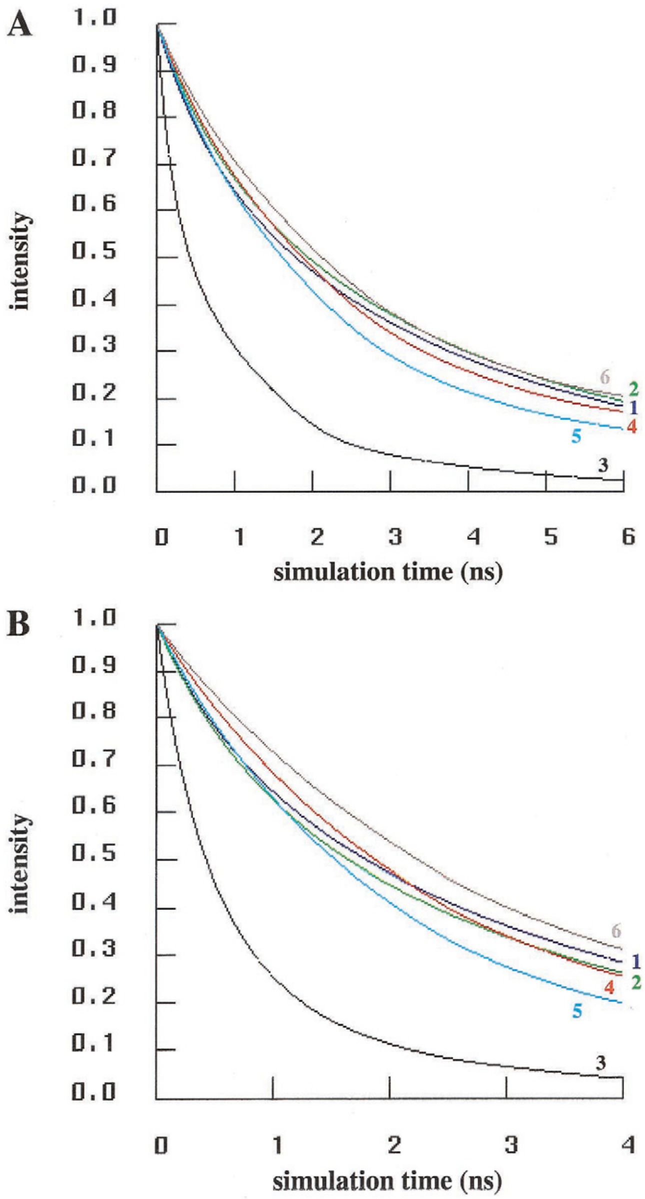

FIGURE 11 Comparison of experimental and simulated fluorescence intensity decays. (*A*) in the absence of Mg^{2+}. (*B*) In the presence of Mg^{2+}. *Curves 1 and 2*, experimental decays $I_e(t)$ from Eq. 1 at 5°C and at 30°C, respectively. *Curve 3*, simulated decay with $\tau_{\mathrm{rad}} = 20$ ns, $k_0 = 25\ \mathrm{ns}^{-1}$, $\beta = 1.9\ \mathrm{\AA}^{-1}$, favorable $S_{\mathrm{D \rightarrow A}} = 641{,}000\ \mathrm{\AA}^6$/ns and unfavorable $S_{\mathrm{D \rightarrow A}} = 133{,}000\ \mathrm{\AA}^6$/ns. *Curve 4*, best fit of the experimental intensity decay at 5°C using $\tau_{\mathrm{rad}} = 20$ ns, $\beta = 1.9\ \mathrm{\AA}^{-1}$, favorable $S_{\mathrm{D \rightarrow A}} = 6410\ \mathrm{\AA}^6$/ns and unfavorable $S_{\mathrm{D \rightarrow A}} = 1330\ \mathrm{\AA}^6$/ns. (*A*) curve 4, $k_0 = 3.7\ \mathrm{ns}^{-1}$; (*B*) curve 4, $k_0 = 4.6\ \mathrm{ns}^{-1}$. (*A*) and (*B*) curve 5, same parameters as curve 4, except $\beta = 1.7\ \mathrm{\AA}^{-1}$. (*A*) and (*B*) curve 6, same parameters as curve 4, except $\beta = 2.1\ \mathrm{\AA}^{-1}$.

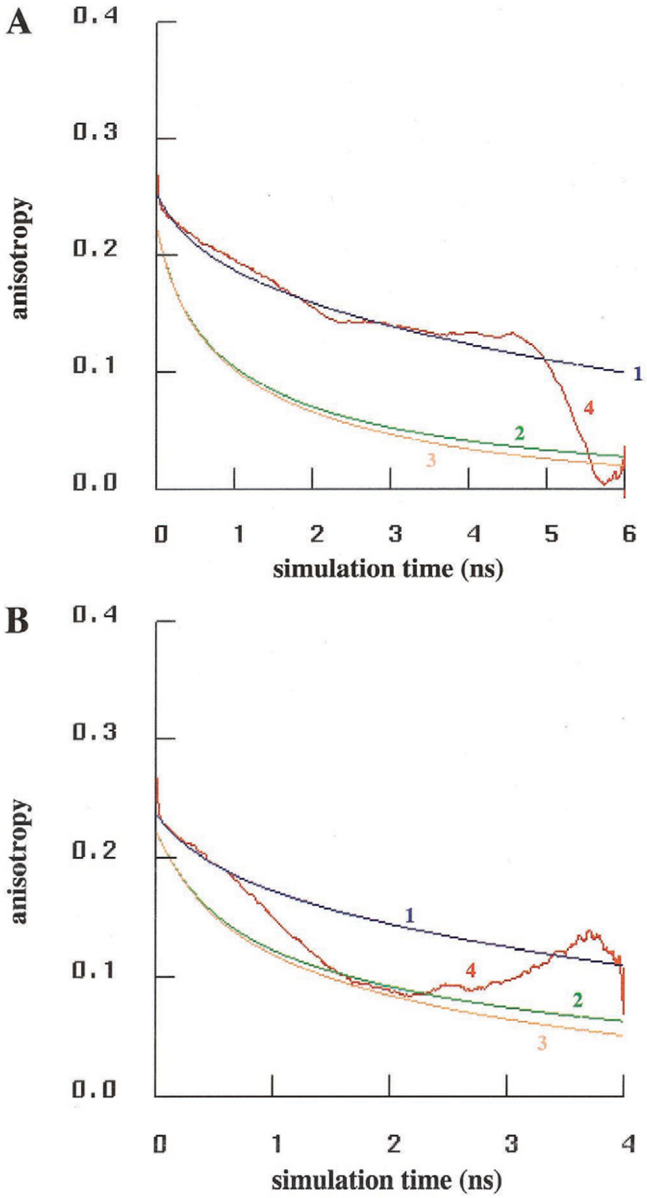

FIGURE 12 Comparison of experimental and simulated fluorescence anisotropy decays. (*A*) In the absence of Mg^{2+}. (*B*) In the presence of Mg^{2+}. *Curves 1 and 2*, experimental decays $r_e(t)$ from Eq. 2 at 5°C and 30°C, respectively. The experimental $r(0)$ were 0.252 at 5°C and 0.223 at 30°C in the absence of Mg^{2+}. The experimental $r(0)$ were 0.237 at 5°C and 0.221 at 30°C in the presence of Mg^{2+}. *Curve 3*, same as curve 2 with the longest anisotropy correlation times divided by 2. *Curve 4*, simulated anisotropy decay using $\tau_{\mathrm{rad}} = 20$ ns, $\beta = 1.9\ \mathrm{\AA}^{-1}$, favorable $S_{\mathrm{D \rightarrow A}} = 6410\ \mathrm{\AA}^6$/ns and unfavorable $S_{\mathrm{D \rightarrow A}} = 1330\ \mathrm{\AA}^6$/ns. (*A*) curve 4, $k_0 = 3.7\ \mathrm{ns}^{-1}$ and (*B*) curve 4, $k_0 = 4.6\ \mathrm{ns}^{-1}$.

hinges, have been replaced by alanine residues (Greenwald et al., 1999). The mutants are catalytically impaired. The most likely explanation is that the loop remains flexible in the presence of Mg^{2+} but the motions are probably too slow to be detected using a 4-ns simulation.

The fluorescence intensity and anisotropy decays were computed from the MD simulation and compared to the experimental decays. The simulation fluorescence study was not limited to the computation of the instantaneous lifetimes of Trp residues, but the excitation history was followed frame after frame from absorption until de-excitation time. The decays were built by averaging over the absorption time. The procedure used here shows how the instantaneous lifetimes, that can be computed from electron or proton transfers in a given conformation, are modulated by the speed of the protein internal motions. If the instantaneous lifetimes were much longer than the time characterizing their changes, they would be equal to the lifetimes of the fluorescence intensity decay. In contrast, if the internal motions were very rapid, the instantaneous lifetimes would change very rapidly. In that extreme case, the intensity decay would be a unique exponential. The inverse of the unique lifetime would be the average of all the instantaneous lifetime inverse values. The case of HIV-1 IN catalytic core is intermediate.

In this work, the Trp natural fluorescence lifetime is modulated by the electron transfer from CE3 to the nearest C atom of the adjacent residues along the chain. We can add here that we also tried a through space model. In such a model, the Trp electron is allowed to jump through space to any C atom. Quenching is then too strong and we were not able to fit the experimental intensity decays.

The fluorescence intensity and anisotropy decays depend on relatively few parameters. Each parameter has a different influence on the fit to the experimental data. For instance, the radiative lifetimes had no influence on the simulated decay but, again, this may come from the length of our simulation. The parameters we had to modify are the rate of electron transfer and the spectral parameter for energy transfers, and, once more, the best-fitting values depend on the size of the analyzed data. The energy transfer spectral parameter that fits the data is 100 times less than the values reported by Willaert et al. (1992). This may come from many different causes: environment of the Trp residues, differences in the excitation wavelengths (295 versus 299 nm). In contrast, the parameter β was in agreement with recent work (Sillen et al., 2000) and was slightly smaller than older values obtained in α helices and β sheets (Beratan and Skourtis, 1998). The experimental anisotropy at time 0, $r(0)$, is 0.22, which is very far from the expected value of 0.4 if both excitation and emission transition moments of Trp were identical. But so low a value is common in proteins. For instance, in experimental conditions that are close to ours (excitation wavelength 300 nm, temperature 20°C), $r(0)$ is 0.22 for liver alcohol dehydrogenase, a dimeric protein containing two Trp residues in each subunit (Ross et al., 1981). The low value of $r(0)$ may have different causes (Tanaka et al., 1994). In this work, the simulated anisotropy was shown to decrease very rapidly in the first 0.1 ps. The experimental value of $r(0)$ can significantly differ from the fundamental r_0 if the time response of the detecting apparatus is not short enough. The fit was not significantly improved when a small partial overlap between the ^1L_a and ^1L_b excited electronic bands in Trp was introduced, which was expected, because, when the excitation wavelength is 299 nm, the proportion of Trp residues excited in ^1L_b is certainly small.

To compute the decays, it was necessary to estimate the energy transfer rates. It is impressive how rapidly these rates change with time at the 0.1-ps scale. This may be correlated with the large fluctuations observed in measurements done on single molecules (Moerner and Orrit, 1999). Interestingly, these very rapid fluctuations are averaged in the method used here. Finally, the fluctuations do not imply that their history should be followed at a very high time resolution. It is, however, important to sample a large number of snapshots.

The fit of the anisotropy decay at 5°C was really good. In contrast, the anisotropy decay at 30°C could not be fitted even when the resonance energy transfers within a chimeric dimer were taken into account with the same parameters as at 5°C. Several factors may contribute to the lack of fit. First, an actual dimer should have been considered, not a chimeric one. In a chimeric dimer, the internal motions of both subunits are identical. In an actual dimer, the internal motions might be drastically disparate. Second, the transfer efficiency may depend on temperature. Third, the catalytic core may dimerize differently in diluted aqueous solution and in the crystal structures. In all known structures, cysteine residues are too distant from each other to form disulfide bridges. Yet, IN oligomers have been detected, in which formation was dependent on disulfide bridges (Petit et al., 1999).

The calculation of intensity and anisotropy decays as described in this work can be extended to any protein, regardless of the number of Trp, because most of the deexcitation processes are taken into account. To gain better predictions of the fluorescence properties, all the possible conformations of Trp should be scanned, which requires longer dynamics and is limited by computational power and data-storage facilities. In addition, this protocol can be extended to gain insight into the conformation of IN-inhibitor complexes. Some of the styrylquinoline derivatives are IN-inhibitors (Mekouar et al., 1998; Zouhiri et al., 2000) and are very weakly fluorescent with an excitation band in the 330–350-nm range (Ouali et al., 2000a). Using docking procedures, these inhibitors were shown to bind to the catalytic core of the related RSV IN in the vicinity of the catalytic Mg^{2+} cation (Ouali et al., 2000b). Fluorescence simulation of IN complexes with such fluorescent drug is then possible just by adding the computation of the Trp-inhibitor heterotransfer.

APPENDIX: MATRIX EXPONENTIAL

The exponential E of the matrix K is

$$E = \exp K = 1 + K + K^2/2! + \cdots + K^m/m! + \cdots. \tag{A1}$$

The series can be truncated at the third or fourth term when K is small, as has been usually the case here. This formula is rapid and easy to implement, but gives only an approximation of E. If the matrix K can be set into diagonal form, L, with eigenvalues λ_i (sorted by increasing order $\lambda_1 \leq \lambda_2 \leq \cdots \leq \lambda_N$) using an inversible matrix P, then L is defined by

$$L = P^{-1}KP. \tag{A2}$$

If F defines a diagonal matrix with ith diagonal elements,

$$F_{ii} = \exp \lambda_i, \tag{A3}$$

then E is exactly given by

$$E = PFP^{-1}. \tag{A4}$$

During the diagonalization of K, it is always possible to zero the upper part of L, that is, the elements L_{ij} with $j > i$. However, when K is not symmetric and when several diagonal terms λ_i and λ_j are equal to a common value λ, it may occur that the term L_{ji} does not vanish. In that case, L can only be written as a lower triangle. If there are at most four identical eigenvalues, straightforward algebra leads to the exponential of L as the matrix F:

$$F = \begin{pmatrix} 1 & 0 & 0 & 0 \\ L_{21} & 1 & 0 & 0 \\ L_{31} + \dfrac{L_{32}L_{21}}{2} & L_{32} & 1 & 0 \\ L_{41} + \dfrac{L_{42}L_{21} + L_{43}L_{31}}{2} + \dfrac{L_{43}L_{32}L_{21}}{6} & L_{42} + \dfrac{L_{43}L_{32}}{2} & L_{43} & 1 \end{pmatrix} \cdot \exp \lambda, \tag{A5}$$

and E is given by Eq. A4. For the matrices considered in this work, the exact and the truncated series results were identical to the fourth significant digit.

Parameter optimization is easier if the gradient of the function to be fitted is available. Here, it requires the adaptation of the algorithm concerning the gradient of the exponential of symmetric matrices (Pothier et al., 1993). This is postponed to a later work. In this work, parameter optimization has been done by trial and error. Each decay simulation from the 6-ns MD contained 60,000 intensity and anisotropy points, which, as a whole, required approximately 1.8×10^9 matrix multiplications. The CPU time was 24 hours on a single SGI R10000 processor. Therefore, only 30 different sets of parameters have been tried.

This work has been made possible through access to the SGI/O2000 multiprocessor of the Pôle Parallélisme IdF Sud. It has been supported by Centre National de la Recherche Scientifique, Agence Nationale pour la Recherche contre le SIDA and SIDACTION.

C.L., E.D., and H.L. are grateful for MENRT, SIDACTION, and Bioalliance fellowships, respectively. Drs. Mahmoud Roshani and Patrick Tauc are thanked for skillful assistance.

REFERENCES

Andrake, M. D., and A. M. Skalka. 1996. Retroviral integrase, putting the pieces together. *J. Biol. Chem.* 271:19633–19636.

Aqvist, J. 1990. Ion–water interaction potentials derived from free energy perturbation simulations. *J. Phys. Chem.* 94:8021–8024.

Beratan, D. N., and S. S. Skourtis. 1998. Electron transfer mechanisms. *Curr. Opin. Chem. Biol.* 2:235–243.

Brochon, J. C. 1994. Maximum entropy method of data analysis in time-resolved spectroscopy. *Methods Enzymol.* 240:262–311.

Brown, P. O. 1990. Integration of retroviral DNA. *Curr. Top. Microbiol. Immunol.* 157:19–48.

Brown, P. O. 1997. *In* Retroviruses. S. Coffin, S. H. Hughes, and H. E. Varmus, editors. Cold Spring Harbor Lab Press, Plainview, NY. 161–203.

Bujacz, G., M. Jaskolki, J. Alexandratos, A. Wlodawer, G. Merkel, R. A. Katz, and A. M. Skalka. 1995. High-resolution structure of the catalytic domain of avian sarcoma virus integrase. *J. Mol. Biol.* 253:333–346.

Bujacz, G., J. Alexandrakos, Q. Zhou-Liu, C. Clément-Mella, and A. Wlodawer. 1996. The catalytic domain of human immunodefficiency virus integrase: ordered active site of the F185H mutant. *FEBS Lett.* 398:175–178.

Bushman, F. D., T. Fujiwara, and R. Craigie. 1990. Retroviral DNA integration directed by HIV integration protein in vitro. *Science.* 249: 1555–1558.

Bushman, F. D., and R. Craigie. 1991. Activities of human immunodefficiency virus (HIV) integration protein in vitro: specific cleavage and integration of HIV DNA. *Proc. Natl. Acad. Sci. U.S.A.* 88:1339–1343.

Callis, P. 1997. ^1L_a and ^1L_b transitions of tryptophan: applications of theory and experimental observations to fluorescence of proteins. *Methods Enzymol.* 278:113–150.

Callis, P., and B. Burgess. 1997. Tryptophan fluorescence shifts in proteins from hybrid simulations: an electrostatic approach. *J. Phys. Chem.* 101:9429–9432.

Chen, J., J. Krucinski, L. Miercke, J. Finer-Moore, A. Tang, A. Leavitt, and R. Stroud. 2000. Crystal structure of the HIV-1 integrase catalytic core and C-terminal domains: a model for viral DNA binding. *Proc. Natl. Acad. Sci. U.S.A.* 97:8233–8238.

Chen, Y., and M. D. Barkley. 1998. Toward understanding tryptophan fluorescence in proteins. *Biochemistry.* 37:9976–9982.

Chen, Y., B. Liu, H. Yu, and M. D. Barkley. 1996. The peptide bond quenches indole fluorescence. *J. Am. Chem. Soc.* 118:9271–9278.

Chow, S. A., K. A. Vincent, V. Ellison, and P. O. Brown. 1992. Reversal of integration and DNA splicing mediated by integrase of human defficiency virus. *Science.* 255:723–726.

Cornell, W. D., P. Cieplak, C. I. Bayly, I. R. Goulg, K. M. Merz, D. M. Ferguson, D. C. Spellmeyer, T. Fox, J. W. Caldwell, and P. A. Kollman. 1995. A second generation force field for the simulation of proteins, nucleic acids, and organic molecules. *J. Am. Chem. Soc.* 117: 5179–5197.

Darden, T., D. York, and L. Pedersen. 1993. Particle mesh Ewald: An $N \cdot \log(N)$ method for Ewald sums in large systems. *J. Chem. Phys.* 98: 10089–10092.

Deprez, E., P. Tauc, H. Leh, J. F. Moucadet, C. Auclair, and J. C. Brochon. 2000. Oligomeric states of the HIV-1 integrase as measured by time-resolved fluorescence anisotropy. *Biochemistry.* 39:9275–9284.

Doniach, S., and P. Eastman. 1999. Protein dynamics simulations from nanoseconds to microseconds. *Curr. Opin. Struct. Biol.* 9:157–163.

Ewald, P. 1921. Die Berechnung optischer und elektrostatischer Gitterpotentiale. *Ann. Phys.* 64:253–287.

Förster, T. 1948. Zwischenmolekulare Energiewanderung und Fluoreszenz. *Ann. Phys. (Leipzig).* 2:55–75.

Frisch, M., G. Trucks, H. Schlegel, G. Scuseria, M. Robb, J. Cheeseman, V. Zakrzewski, J. Montgomery, R. Stratmann, J. Burant, S. Dapprich, J. Millam, A. Daniels, K. Kudin, M. Strain, O. Farkas, J. Tomasi, V. Barone, M. Cossi, R. Cammi, B. Mennucci, C. Pomelli, C. Adamo, S. Clifford, J. Ochterski, G. Petersson, P. Ayala, Q. Cui, K. Morokuma, D. Malick, A. Rabuck, K. Raghavachari, J. Foresman, J. Cioslowski, J. Ortiz, B. Stefanov, G. Liu, A. Liashenko, P. Piskorz, I. Komaromi, R. Gomperts, R. Martin, D. Fox, T. Keith, M. Al-Laham, C. Peng, A. Nanayakkara, C. Gonzalez, M. Challacombe, P. Gill, B. Johnson, W. Chen, M. Wong, J. Andres, C. Gonzalez, M. Head-Gordon, E. Replogle, and J. Pople. 1998. Gaussian 98, Revision A.6. Gaussian, Inc., Pittsburgh, PA.

Goldgur, Y., F. Dyda, A. Hickman, T. Jenkins, R. Craigie, and D. Davies. 1998. Three new structures of the core domain of HIV-1 integrase: an active site that binds magnesium. *Proc. Natl. Acad. Sci. U.S.A.* 95: 9150–9154.

Greenwald, J., V. Le, S. Butler, F. Bushman, and S. Choe. 1999. The mobility of an HIV-1 integrase active site loop is correlated with catalytic activity. *Biochemistry.* 38:8892–8898.

Ichiye, T., and M. Karplus. 1983. Fluorescence depolarization of tryptophan residues in proteins: a molecular dynamics study. *Biochemistry.* 22:2884–2893.

Jenkins, T. M., A. Engelman, R. Ghirlando, and R. Craigie. 1996. A soluble active mutant of HIV-1 integrase: involvement of both the core and carboxyl-terminal domains in multimerization. *J. Biol. Chem.* 271: 7712–7718.

Kabsch, W., and C. Sander. 1983. Dictionary of protein secondary structure: pattern recognition of hydrogen-bonded and geometrical features. *Biopolymers.* 22:2577–2637.

Le Bret, M., J. B. Le Pecq, J. Barbet, and B. P. Roques. 1977. A reexamination of the problem of resonance energy transfer between DNA intercalated chromophores using bisintercalating chromophores. *Nucleic Acids Res.* 4:1361–1379.

Le Bret, M., J. Gabarro-Arpa, J. C. Gilbert, and C. Lemaréchal. 1991. MORCAD, an object-oriented molecular modelling package running on IBM RS/6000 and SGI 4Dxxx workstations. *J. Chim. Phys.* 88: 2489–2496.

Lee, S. P., J. Xiao, J. R. Knutson, M. S. Lewis, and M. K. Han. 1997. Zn^{2+} promotes the self-association of human immunodeficiency virus type-1 integrase in vitro. *Biochemistry.* 36:173–180.

Leh, H., P. Brodin, J. Bischerour, E. Deprez, P. Tauc, J. C. Brochon, E. LeCam, D. Coulaud, C. Auclair, and J. F. Mouscadet. 2000. Determinants of Mg^{2+}-dependendent activities of recombinant human immunodefficiency virus type 1 integrase. *Biochemistry.* 39:9285–9294.

Lins, R. D., J. M. Briggs, T. P. Straatsma, H. A. Carlson, J. Greenwald, S. Choe, and J. A. McCammon. 1999. Molecular dynamics studies on the HIV-1 integrase catalytic domain. *Biophys. J.* 76:2999–3001.

Lins, R. D., T. P. Straatsma, and J. M. Briggs. 2000a. Similarities in the HIV-1 and ASV integrase active sites upon metal cofactor binding. *Biopolymers.* 53:308–315.

Lins, R. D., A. Adesokan, T. A. Soares, and J. M. Briggs. 2000b. Investigations on human immunodeficiency virus type 1 integrase/DNA binding interactions via molecular dynamics and electrostatics calculations. *Pharmacol. Ther.* 85:123–131.

Livesey, A. K., and J. C. Brochon. 1987. Analyzing the distribution of decay constants in pulse-fluorimetry using the maximum entropy method. *Biophys. J.* 52:693–706.

Maignan, S., J. P. Guilloteau, Q. Zhou-Liu, C. Clément-Mella, and V. Mikol. 1998. Crystal structures of the catalytic domain of HIV-1 integrase free and complexed with its metal cofactor: high level of similarity of the active site with other viral integrases. *J. Mol. Biol.* 282:359–368.

Marcus, R. A., and N. Sutin. 1985. Electron transfers in chemistry and biology. *Biochim. Biophys. Acta.* 811:265–322.

Mekouar, K., J. F. Mouscadet, D. Desmaële, F. Subra, H. Leh, D. Savouré, C. Auclair, and J. d'Angelo. 1998. Styrylquinoline derivatives: a new class of potent HIV-1 integrase inhibitors that block HIV-1 replication in CEM cells. *J. Med. Chem.* 41:2846–2857.

Moerner, W., and M. Orrit. 1999. Illuminating single molecules in condensed matter. *Science.* 283:1670–1676.

Ouali, M., C. Laboulais, H. Leh, D. Gill, E. Xhuvani, F. Zouhiri, D. Desmaële, J. d'Angelo, C. Auclair, J. F. Mouscadet, and M. Le Bret. 2000a. Tautomers of styrylquinoline derivatives containing a methoxy substituent: computation of their population in aqueous solution and their interaction with RSV integrase catalytic core. *Acta Biochim. Pol.* 47:11–22.

Ouali, M., C. Laboulais, H. Leh, D. Gill, D. Desmaële, K. Mekouar, F. Zouhiri, J. d'Angelo, C. Auclair, J. F. Mouscadet, and M. Le Bret. 2000b. Modeling of the inhibition of retroviral integrases by styrylquinoline derivatives. *J. Med. Chem.* 43:1949–1957.

Perrin, F. 1929. La fluorescence des solutions. *Ann. de Phys.* 12:169–275.

Petit, C., O. Schwartz, and F. Mammano. 1999. Oligomerization within virions and subcellular localization of human immunodeficiency virus type 1 integrase. *J. Virol.* 73:5079–5088.

Pothier, J., J. Gabarro-Arpa, and M. Le Bret. 1993. MORMIN: a quasi-Newtonian energy minimizer fitting the nuclear overhauser data. *J. Comp. Chem.* 14:226–236.

Ringhofer, S., J. Kallen, R. Dutzler, A. Billich, A. Visser, D. Scholtz, O. Steinhauser, H. Schreiber, M. Auer, and A. Kungl. 1999. X-ray structure and conformation dynamics of the HIV-1 protease in complex with the inhibitor SDZ283–910: agreement of time-resolved spectroscopy and molecular dynamics simulations. *J. Mol. Biol.* 286:1147–1159.

Ross, J. B., C. J. Schmidt, and L. Brand. 1981. Time-resolved fluorescence of the two tryptophans in horse liver alcohol dehydrogenase. *Biochemistry.* 20:4369–4377.

Ryckaert, J. P., G. Cicotti, and H. Berendsen. 1977. Numerical integration of the Cartesian equations of motion of a system with constaints: molecular dynamics of *n*-alkanes. *J. Comp. Phys.* 23:327–341.

Sakai, H., M. Kawamura, J. Sakuragi, S. Sakuragi, R. Shibata, A. Ishimoto, N. Ono, S. Ueda, and A. Adachi. 1993. Integration is essential for efficient gene expression of human immunodeficiency virus type 1. *J. Virol.* 67:1169–1174.

Sillen, A., J. F. Diaz, and Y. Engelborghs. 2000. A step toward the prediction of the fluorescence lifetimes of tryptophan residues in proteins based on structural and spectral data. *Protein Sci.* 9:158–169.

Strickler, S., and R. Berg. 1962. Relationship between absorption intensity and fluorescence lifetime of molecules. *J. Chem. Phys.* 87:814–822.

Szabo, A., and D. Rayner. 1980. Fluorescence decay of tryptophan conformers in aqueous solution. *J. Am. Chem. Soc.* 102:554–563.

Tanaka, F., N. Tamai, N. Mataga, B. Tonomura, and K. Hiromi. 1994. Analysis of internal motion of single tryptophan in *Streptomyces subtilisin* inhibitor from its picosecond time-resolved fluorescence. *Biophys. J.* 67:874–880.

Valeur, B., and G. Weber. 1977. Resolution of the fluorescence excitation spectrum of indole into the ^1L_a and ^1L_b excitation bands. *Photochem. Photobiol.* 25:441–444.

Weber, W., H. Demirdjian, R. D. Lins, J. M. Briggs, R. Ferreira, and J. A. McCammon. 1998. Brownian and essential dynamics studies of the HIV-1 integrase catalytic domain. *J. Biomol. Struct. Dyn.* 16:733–745.

Willaert, K., R. Loewenthal, J. Sancho, M. Froeyen, A. Fersht, and Y. Engelborghs. 1992. Determination of the excited-state lifetimes of tryptophan residues in barnase, via multifrequency phase fluorometry of tryptophan mutants. *Biochemistry.* 31:711–716.

Zheng, R., T. Jenkins, and R. Craigie. 1996. Zinc folds the N-terminal domain of HIV-1 integrase, promotes multimerization, and enhances catalytic activity. *Proc. Natl. Acad. Sci. U.S.A.* 93:13659–13664.

Zouhiri, F., J. F. Mouscadet, K. Mekouar, D. Desmaële, D. Savouré, H. Leh, F. Subra, M. Le Bret, C. Auclair, and J. d'Angelo. 2000. Structure-activity relationships and binding mode of styrylquinolines as potent inhibitors of HIV-1-integrase and replication of HIV-1 in cell culture. *J. Med. Chem.* 43:1533–1540.